Ash and ice clouds during the Mt. Kelud Feb 2014 eruption as interpreted from IASI and AVHRR/3 observations

Arve Kylling[1]

[1]NILU - Norwegian Institute for Air Research, P.O.Box 100, 2027 Kjeller,Norway

Correspondence to: Arve Kylling
(arve.kylling@nilu.no)

Abstract. During the Mt. Kelud Feb 2014 eruption the ash cloud was detectable on 13-14 Feb in the infrared with the reverse absorption technique by, for example, the Advanced Very High Resolution Radiometer (AVHRR/3). The Infrared Atmospheric Sounding Interferometer (IASI) observed the ash cloud also on 15 Feb when AVHRR did not detect any ash signal. The differences between ash detection with AVHRR/3 and IASI are discussed and the reasons for the differences supported with radiative
5 transfer modelling. The effect of conccurent ice clouds on the ash detection and the ash signal in the IASI measurements is demonstrated. Specifically, a radiative transfer model is used to simulate IASI spectra with ash only, with ice cloud only and with both ash and ice clouds. It is shown that modelled IASI spectra with ash and ice clouds better reproduce the measured IASI spectra than ash only or ice only modelled spectra. The ash and ice modelled spectra that best reproduce the IASI spectra contain about a factor of 14 less ash than the ash only spectra that come closest to reproducing the measured spectra.

10 # 1 Introduction

During volcanic eruptions large quantities of ash may be ejected high into the atmosphere. The ash may be observed by both UV-visible and infrared (IR) satellite instruments. While the volcanic ash may be the dominating compound in the atmospheric column viewed by each instrument pixel, it is seldom the sole compound. For example, Maddy et al. (2011) estimated that less than 10% of the footprints of the Infrared Atmospheric Sounding Interferometer (IASI) are expected to be cloud free. Hence,
15 the radiometric signal measured by IASI during a volcanic eruption may have contributions from clouds which impact the volcanic ash signal.

IASI onboard the Meteorologial Operation (MetOp)-A, Metop-B and Metop-C (from 2016) satellites, measures infrared radiation with high spectral resolution. As such it has the potential to provide increased information content compared to spectral band instruments such as AVHRR/3, the Moderate Resolution Imaging Spectroradiometer (MODIS), the Spinning
20 Enhanced Visible and InfraRed Imager (SEVIRI) and the Multifunctional Transport Satellite (MSAT) imager. IASI is dedicated to operational meteorological soundings of temperature and humidity. It may also be used to detect and measure the amount of a number of trace gases (Clerbaux et al., 2009; Hilton et al., 2011). IASI has been succesfully used to detect volcanic ash. In the 800-1200cm^{-1} region silicate absorbers exhibit a characteristic "V" shape (see for example Fig. 2 of Clarisse et al., 2010b). DeSouza-Machado et al. (2006) used this characteristic "V" shape to retrieve the IR optical depth of dust storms as recorded

by the Atmospheric Infrared Sounder (AIRS). Gangale et al. (2010) used the same spectral signature to detect ash in AIRS data. Their concavity algorithm utilizes the spectral behaviour of the brightness temperature in the 800-1130 cm^{-1} range to distingush ash from desert dust and ice and water clouds. They also demonstrated that the concavity increases monotonically with increasing optical depth, thus indicating that concavity may be used to infer particle size and composition. Clarisse et al. (2013) gave an overview of the various methods used for aerosol (and ash) detection from hyperspectral infrared sounders. These methods include feature detection, spectral fitting, distance approaches, singular value decomposition and principal component analysis, and methods utilizing geophysical information.

The aims of the present study are to 1) investigate the combined impact of ash and water ice clouds on IASI Metop-A spectra using radiative transfer modelling, and 2) find the combination of ash and ice clouds that best reproduce the spectra measured during the Mt. Kelud 2014 eruption. In addition to IASI data, measurements from AVHRR/3, also onboard Metop-A, are used.

2 Mt. Kelud Feb 2014 eruption

Mt. Kelud, Indonesia, erupted on 13 Feb, 2014 at 2250 local time (UT+7). The explosive eruption declined the following days and on 21 Feb the volcano's alert status was downgraded. The eruption was detected in data from several satellite instruments including IR data from the geostationary MTSAT imager using IR channels similar to the AVHRR/3 instrument (Kristiansen et al., 2015). The satellite imagery showed that the ash cloud from the Mt. Kelud eruption thinned quickly and after 14 Feb the ash cloud was no longer visible close to the volcano in IR data using the reverse absorption technique (Kristiansen et al., 2015; Prata, 1989).

3 IASI and AVHRR data

Both the IASI and AVHRR/3 instruments onboard the polar orbiting MetOp-A the polar orbiting satellite observed the Mt. Kelud 2014 ash cloud.

3.1 The Advanced Very High Resolution Radiometer (AVHRR/3)

AVHRR/3 has three solar and three thermal channels and a spatial resolution of 1.1 km at nadir. The AVHRR/3 thermal channels 4 and 5 are centered at 10.8 and 12.0 μm, respectively, and may be used for detection of volcanic ash by the reverse absorption technique (Prata, 1989; Wen and Rose, 1994). The brightness temperature difference (BTD) between AVHRR/3 channels 4 and 5 is shown in the left plots of Figs. 1 and 2. By the reverse absorption technique volcanic ash affected pixels are identified by looking for pixels with BTD less than some threshold value, typically set between -0.5 and -1. For 14 Feb 2014, 0253 UTC there is an area between 7-10°S and 106-110°E where $BTD < -0.5$, left plot Fig. 1. The pixels within this area are thus identified as ash affected. The BTD for 15 Feb 2014, 0229-0235 UTC, is shown in the left plot of Fig. 2. Less than 0.001% of the pixels in this plot have $BTD < -0.5$ and they are scattered around. Hence, no ash is identified by AVHRR/3 in this image similar to what is reported from MTSAT observations for this date by Kristiansen et al. (2015).
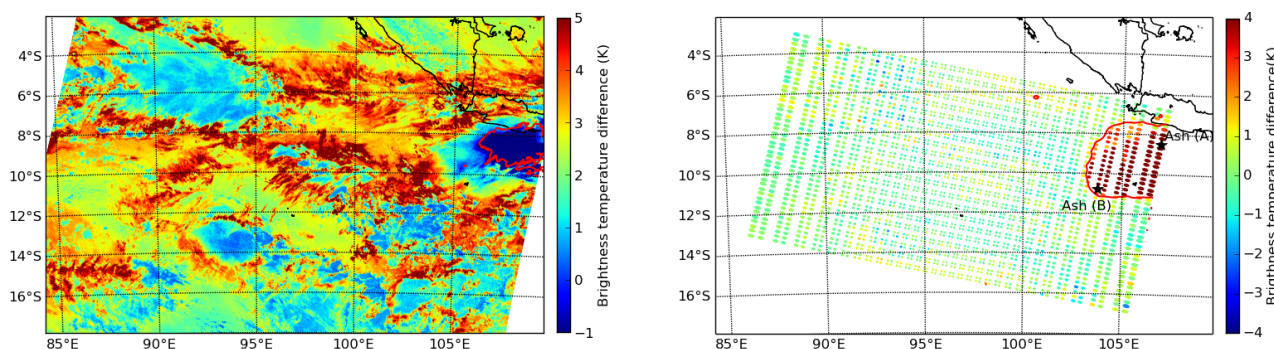
Figure 1. (Left plot) The brightness temperature difference between AVHRR/3 channels 4 and 5 ($BTD_A = BT_4 - BT_5$). The contour line (red) is at -0.5 K. (Right plot) The 1231.5-1097.25 cm^{-1} brightness temperature difference from IASI/Metop-A spectra. The contour line is at 1.5 K. Data from 14 Feb 2014, 0253 UTC.

3.2 The Infrared Atmospheric Sounding Interferometer (IASI)

IASI covers the spectral range from 645 to 2760 cm^{-1} (15.50-3.6 μm). The spectral resolution varies with wavelength and lies between 0.3-0.5 cm^{-1}. The Level 1C products have spectral resolution of 0.5 cm^{-1} and are sampled every 0.25 cm^{-1}. This gives a total of 8461 radiance values per spectrum (Clerbaux et al., 2009). For the wavenumber interval exploited here, 700-1250 cm^{-1}, the noise equivalent temperature difference is less than 0.2 K (Table 1, Clerbaux et al., 2009). Each spectrum represents a circular footprint with diameter of 12 km at nadir. At the swath edges the footprint is roughly elliptical with axes of 39 km (across track) and 20 km (along track) (Clarisse et al., 2011). The spatial resolution of AVHRR/3 is about 1.1 km. Hence one IASI footprint is covered by approximately 90 AVHRR/3 pixels.

Due to the larger spectral coverage and higher spectral resolution several approaches may be used to detect volcanic ash with IASI (Clarisse et al., 2013). A simple brightness temperature difference scheme defined as the brightness temperature difference between the channels at 1231.5 and 1168 cm^{-1} was used by Clarisse et al. (2010a). This approach is based on the characteristic "V" shape (see for example Fig. 2 of Clarisse et al., 2010b) of silicate absorbers in the 800-1250cm^{-1} region. A pixel is said to contain ash if the brightness temperature is larger than some threshold value, 0.5 K was used by Clarisse et al. (2010a).

However, the 1168 cm^{-1} channel may be affected by absorption in the symmetric stretch ν_1 band of SO$_2$ which covers the 1070-1230 cm^{-1} region, see left plot of Fig. 3. The channel at 1097.25 cm^{-1} is little affected by SO$_2$ ν_1 absorption. To estimate the SO$_2$ effect on this channel radiative transfer simulations (described in further detail in section 4) were made. First a simulation with a background SO$_2$ column of 0.13 DU and no ash were made, giving BTD_I=BT$_{1231.5}$-BT$_{1097.25}$=-0.31 K. Next SO$_2$ clouds were introduced between 17-19 km with total column densities of 10 and 100 DU. In the left plot
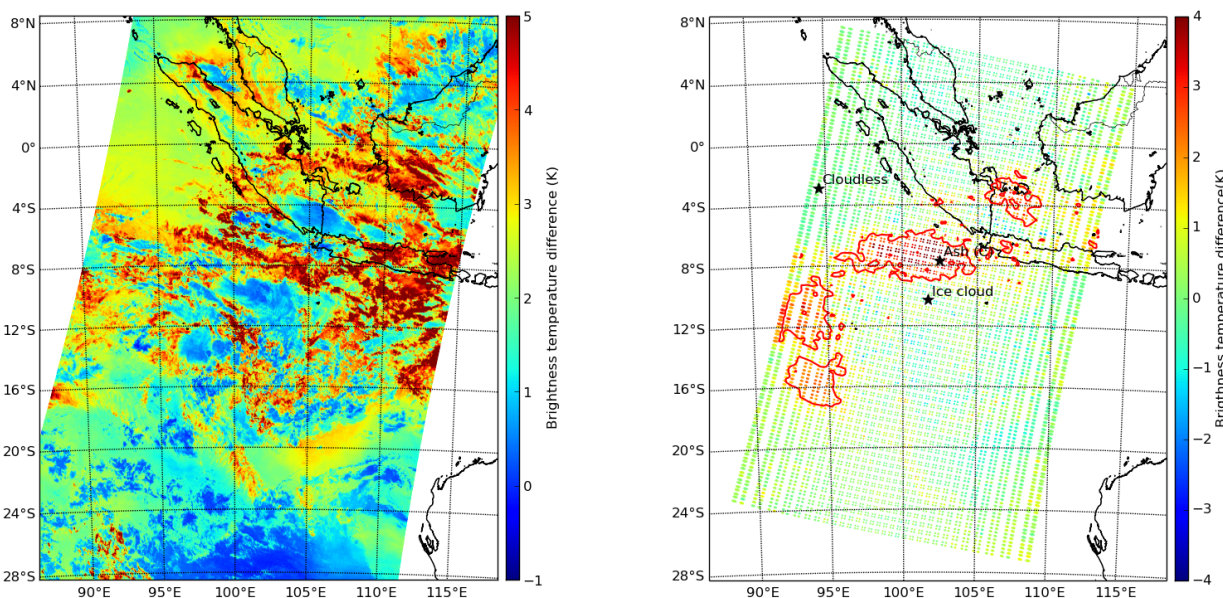
Figure 2. (Left plot) The brightness temperature difference between AVHRR/3 channels 4 and 5 ($BTD_A = BT_4 - BT_5$). (Right plot) The 1231.5-1097.25 cm^{-1} brightness temperature difference from IASI/Metop-A spectra. The contour line is at 1.5 K. Data from 15 Feb 2014, 0229-0235 UTC.

of Fig. 3 is shown the difference between spectra with background SO$_2$ and the spectra with 10 and 100 DU. An SO$_2$ column of 10 (100) DU gives BTD_I=-0.99 (-0.47) K implying that the 1231.5 and 1097.25 cm^{-1} channel differences do not become positive for realistic SO$_2$ amounts.

Alas, using the 1097.25 cm^{-1} channel instead of the 1168.25 cm^{-1} channel implies that the wavelength dependence of
5   the refractive index of water ice may have an effect if ice clouds are present somewhere in the same atmospheric column as the ash cloud. Further radiative transfer simulations were made to assess this effect. In the right plot of Fig. 3 is shown the simulated 1231.5-1097.25 cm^{-1} brightness temperature difference as a function of ice water content and ice cloud top height. The water ice cloud was 1 km thick. From Fig. 3 it is clear that BTD_I=BT$_{1231.5}$-BT$_{1097.25}$ becomes larger than 1.5 K for ice clouds at altitudes greater than about 15 km and ice water contents around 0.1 g/cm^3. For the episode under investigation
10   here, CALIOP (Cloud-Aerosol Lidar with Orthogonal Polarization) data shows that cirrus cloud were present below 15 km (see Fig. 2e Kristiansen et al., 2015). Hence to minimize the effect of absorption by SO$_2$ and the effect of ice clouds on ash detection it is required that BTD_I=BT$_{1231.5}$-BT$_{1097.25}$ > 1.5 K.

In the right plots of Figs. 1 and 2 BTD_I is shown including a contour line at 1.5 K. For 14 Feb 2014, 0253 UTC the area identified as ash by IASI overlaps with the area detected by AVHRR/3 (left plot) but is somewhat larger. For 15 Feb 2014,
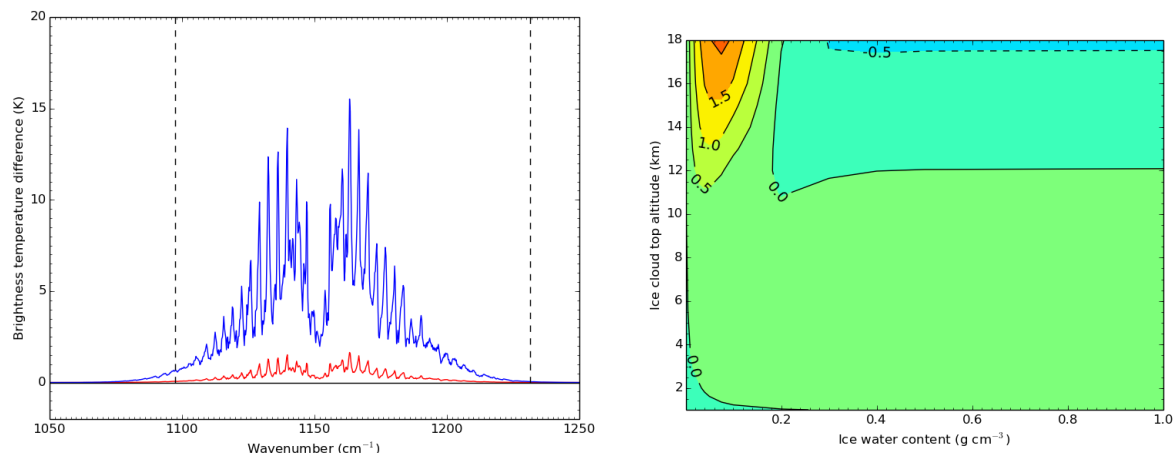
Figure 3. (Left plot) The difference between a spectrum with background SO_2 and with a SO_2 plume between 17-19 km giving a total column of 10 (100) DU, red (blue) line. (Right plot) The 1231.5-1097.25 cm^{-1} brightness temperature difference (K) for a horizontal water ice cloud of 1 km thickness as a function of ice cloud top height and ice water content.

0229-0235 UTC, Fig. 2, IASI detects ash whereas AVHRR/3 does not. To further understand why ash is identified by IASI and not AVHRR/3, IASI spectra between 700-1225 cm^{-1} shown in Fig. 4 with locations marked by black stars in the right plots of Figs. 1 and 2, and listed in Table 1, are investigated in detail using radiative transfer modelling.

Table 1. Information pertinent to IASI data shown in Fig. 4. BTD_I is the brightness temperature difference between the channels at 1231.5 and 1097.25 cm^{-1}. BT_4 is the mean AVHRR channel 4 brightness temperature for the AVHRR pixels covering the IASI footprint, and σ_{BT_4} the standard deviation. The brigthness temperature difference between the means of AVHRR channels 4 and 5, $BTD_A = BT_4 - BT_5$. is given in column 7. AML denotes the ash mass loading, IWC is the ice water content and ICT the ice cloud top height. RMSD is defined in Eq. 1.

Day	Time	Latitude	Longitude	BTD_I	BT_4	σ_{BT_4}	BTD_A	AML	r_{eff}	IWC	ICT	RMSD	Comments
(dd)	(hhmm)	(°)	(°)	(K)	(K)	(K)	(K)	(g/m³)	(µm)	(g/m³)	(km)	(K)	
14	0254	-8.47211	106.89724	17.02	226.0	2.6	-4.45	0.0025	1.0	0.075	14.0	1.52	Ash (A)
14	0254	-10.75264	103.74948	5.84	263.6	3.5	4.35	0.0005	3.0	0.03	17.0	0.55	Ash (B)
15	0232	-2.82008	94.51644	-0.15	294.1	0.1	2.63	0.0	-	0.001	16.0	0.59	Cloudless
15	0232	-7.6605	102.47361	4.11	246.4	6.0	4.38	0.001	4.0	0.05	16.0	0.67	Ash (C)
15	0232	-10.28912	101.70977	0.24	202.8	1.1	0.56	0.0	-	0.2	16.0	1.39	Ice cloud
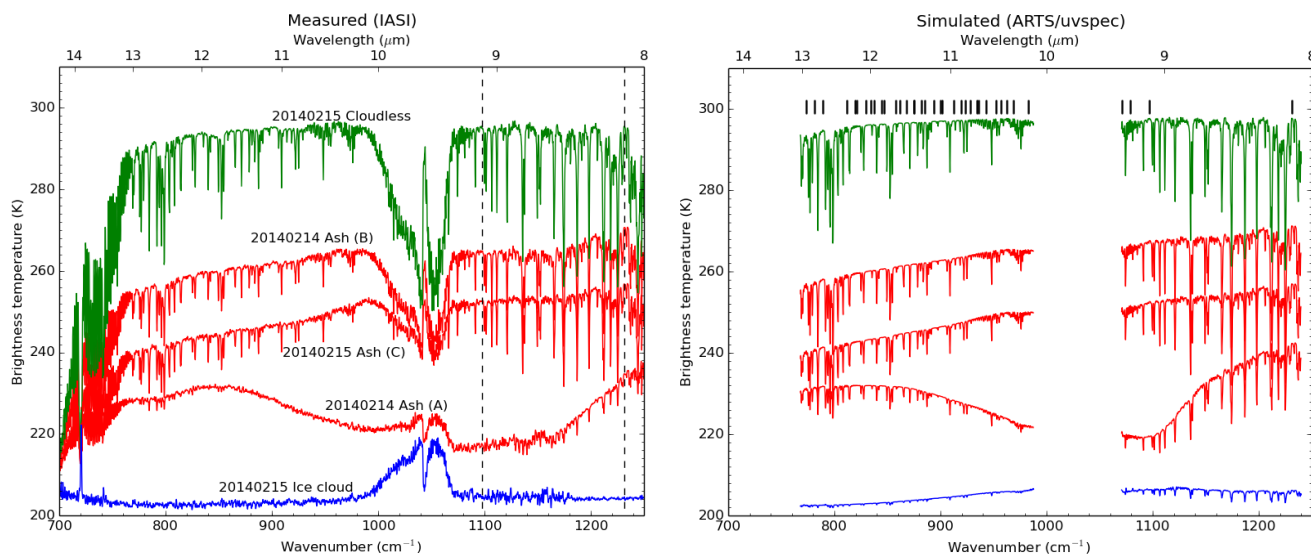
Figure 4. (Left plot) Measured IASI/Metop-A spectra for the pixels marked in the right plots of Figs. 1 and 2, and listed in Table 1. The dashed vertical lines are at 1231.5 and 1097.25 cm^{-1}, the wavelengths used to calculate BTD_I. (Right plot) IASI spectra simulated by ARTS/uvspec. The regions affected by ozone, between about 988-1070 cm^{-1}, and carbon dioxide absorption, below about 768 cm^{-1}, have been omitted for clarity. The black vertical lines indicate the wavelengths used in the estimation of ash and ice contents. See section 4.2 for further details.

4 Radiative transfer modelling

IASI spectra were simulated by first calculating line-by-line gaseous absorption optical depths by the Atmospheric Radiative Transfer Simulator (ARTS) model (Eriksson et al., 2011). Next, the gaseous absorption optical depths were used as input to the uvspec radiative transfer model (Mayer and Kylling, 2005; Emde et al., 2015). In addition to gaseous absorption, water ice
5   clouds and volcanic ash clouds were added as described below.

4.1 Individual spectra

Vertical profiles of temperature, pressure, H_2O, O_3, CH_4, N_2O, and CO_2 were obtained from non-cloudy retrievals in the L2 product from IASI (Schlüssel et al., 2005) for the scene from 15 Feb 2014. Atmospheric profiles for temperature, pressure and each trace gas, were made by averaging all the non-cloudy profiles. The parts of the scenes containing ash are mostly over
10   water, hence the surface emissivity was set equal to sea water with values taken from http://www.icess.ucsb.edu/modis/EMIS/ html/seawater.html (the measurement procedure is described in Snyder et al., 1997). No topography was included.

CALIOP data indicate that the ash plume over the vent reached altitudes between 17-26 km. Other clouds were present between 10-15 km, (see Fig. 2e Kristiansen et al., 2015). The IASI scenes investigated here were recorded one and two days

after the CALIOP overpass. We assume that the transported ash cloud is between 17-18 km of altitude. This assumption is supported by dispersion model simulations, Kristiansen et al. (see Figs. 2c and 3b 2015). For the ash the refractive index of andesite from Pollack et al. (1973) was used. The ash particles were assumed to be spherical and to have a lognormal size distribution with geometric standard deviation of 2.0. The ash cloud was assumed to be vertically homogeneous and the ash

5 mass loading and the ash particle radius were varied.

For the simulations with an ice cloud, the ice cloud was assumed to be 1 km thick and vertically homogeneous. The ice particles were assumed to consist of solid columns with r_{eff}=40.0 μm. The optical properties were taken from Yang et al. (2000) and processed as described by Key et al. (2002). The ice cloud altitude and the ice water content were varied.

4.2 Ash and water ice cloud properties

10 Measured spectra were compared with simulated spectra to get an estimate of the ash mass loading, ash particle radius, ice water content and ash cloud altitude. However, the measured IASI spectra contain numerous trace gas absorption lines. The ash and ice optical properties vary comparatively slowly with wavelength, hence only wavelengths for which trace gases have minimal influence were selected to estimate the ash and ice cloud properties. Initially a total of 77 IASI channels were selected from the brightest channel per interval of 5 cm^{-1} in the ranges 770-985 cm^{-1} and 1070-1240 cm^{-1} following Clarisse et al.

15 (2010b). Visual comparisons of measured and simulated spectra and excluding the region between 1097.25 and 1231.25 cm^{-1} possibly affected by SO$_2$, further decreased the number of channels to 37. The location of these wavelengths is shown in the right plot of Fig. 4 as black vertical lines.

Spectra were simulated for three cases:

    – **Ice cloud only:** The ice cloud top height was taken to be 8, 8.5, 9, 9.5, 10, 10.5, 11, 11.5, 12, 12.5, 13., 13.5, 14, 14.5,
20   15, 16, 17, and 18 km. For each altitude the ice water content was 0.001, 0.002, 0.005, 0.01, 0.0125, 0.015, 0.02, 0.03, 0.04, 0.05, 0.075, 0.1, 0.2, 0.3, 0.4, 0.5, 1.0 g/m^3.

    – **Ash cloud only:** The ash cloud top was at 18 km. Ash mass concentrations of 0.0001, 0.00025, 0.0005, 0.00075, 0.001, 0.0015, 0.002, 0.0025, 0.003, 0.0035, 0.004, 0.005, 0.006, 0.007, 0.008, 0.009, 0.010, 0.02, 0.03, 0.05, 0.75, 0.1, 0.5 and 1.0 g/m^3 and ash cloud effective particle radii of 1, 2, 3, and 4 μm were considered.

25   – **Ash cloud and ice cloud.** This case included an ash cloud with top at 18 km and ice clouds as specified for the ice cloud only case. The ice water content was varied as for the ice cloud only case and the ash mass loading and effective radius as for the ash cloud only case.

A total of 306 "ice cloud only", 96 "ash cloud only", and 29376 "ash cloud and ice cloud" spectra were calculated.

For a measured spectrum the brightness temperature was extracted for the $n = 37$ wavelengths described above, and the root
30 mean square difference (RMSD) was calculated

$$\mathrm{RMSD} = \sqrt{\frac{\sum_{i=1}^{n}(y_i^m - y_i^s)^2}{n}}, \tag{1}$$

where y_m and y_s are the measured and the simulated spectra, respectively. The ash and ice cloud used for the simulated spectrum with the smallest RMSD was said to represent the atmospheric state reflected in the measured spectrum. The "ash cloud only" and "ash cloud and ice cloud" cases were included in the estimate only for pixels identified as ash.

5 Results

Both analysis of individual spectra and complete scenes were made to better understand the effect of ice and ash clouds on the measured spectra. But first examples of the effects of ash and water ice clouds on IASI brightness temperatures are demonstrated.

5.1 Ash and ice cloud radiative effects

In the left plot of Fig. 5 is shown the brightness temperature at 773.5 cm^{-1} as a function of ice water content for ice clouds at various altitudes. The brightness temperature decreases with increasing ice water content and increasing ice cloud altitude. The
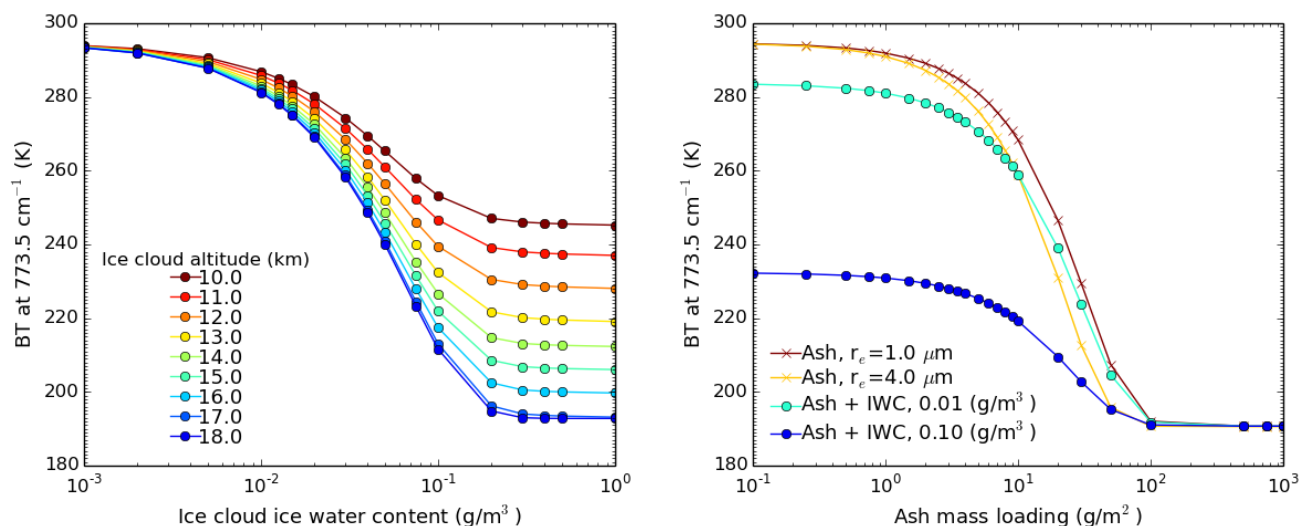
Figure 5. (Left plot) The brightness temperature at 773.5 cm^{-1} as a function of ice water content for ice clouds at various altitudes. (Right plot) The 773.5 cm^{-1} brightness temperature as a function of ash mass loading for pure ash cloud (lines with crosses) with effective radii $r_e = 1.0, 4.0\mu$m, and an ash cloud with $r_e = 1.0\mu$m overlying an ice cloud at 13 km with IWC=0.01 and 0.1 g/m^3 (lines with circles).

cloud becomes opaque at about 0.3 g/m^3 for all ice cloud altitudes and the brightness temperatures then reflects the ambient temperature.

In the right plot of Fig. 5 is shown the brightness temperatures for various ash clouds and ash and ice clouds in combination. The brightness temperature for an effective ash particle radius $r_e = 1.0\mu$m (red line), decrease with increasing ash mass loading

and saturates for an ash mass loading of about 100 g/m^2. For a larger particle radius, $r_e = 4.0 \mu$m (yellow line), the brightness temperature saturates at a slightly smaller mass loading. Including an ice cloud at 13 km below the ash cloud at 18 km (blue and magenta lines) shift the curves towards lower brightness temperatures for ash mass loadings smaller than the saturation value for the ash only case. The leftward shift is larger for denser ice clouds, compare the blue and magenta lines.

5 The behaviour of the brightness temperature will generally be similar for other wavelengths, albeit different in magnitude due to the wavelength dependence of the ice water and ash cloud optical properties. This wavelength dependence is used below to obtain the combination of ash and ice water clouds that best fit the measured spectra.

5.2 Individual spectra

The measured IASI spectra for the star marked locations in the right plots of Figs. 1 and 2 are shown in left plot of Fig. 4. The

10 spectrum identified as ice cloud (blue curve) appears saturated for nearly all wavenumbers except for the ozone band centered around 1050 cm^{-1}. The higher temperatures in the ozone band implies that this radiation was emitted at a higher altitude in the stratosphere where the temperature is higher than at the altitude of the cloud. The rather low and fairly constant overall temperature indicates that this is an ice cloud and that it is opaque. In contrast, the spectrum labelled cloudless (green curve in Fig. 4) have brightness temperatures representative for the ocean at these latitudes. A number of trace gas absorption lines

15 are also readily seen. In the cloudless spectrum the ozone band is colder then the radiation at lower and higher wavenumbers, indicating that the radiation in the ozone band was emitted at a higher and colder altitudes than the surface. The red curves in the left plot of Fig. 4 are identified as ash by the IASI BTD_I method (see also Table 1). These spectra are colder than the cloudless spectrum indicating a colder effective emitting temperature. Between 800-1000 cm^{-1} the ash spectra both increase (spectra B and C) and decrease (spectrum A) with increasing wavenumber. Above about 1200 cm^{-1} the brightness temperature

20 of the cloudless spectrum generally decrease with increasing wavenumber, while the converse is true for the ash spectra. The ice cloud spectrum is spectrally flat except for the ozone band. This behaviour is reflected in BTD_I and BTD_A in Table 1, and explains why IASI identifies ash on 14 and 15 Feb while in the AVHRR/3 data ash is only identified on 14 Feb. This is similar to the behaviour of the spectra from the Eyjafjallajökull eruption discussed by Clarisse et al. (2010b) in their Fig. 2. They present two spectra; one gives negative BTD_A, the other not, while both give $BTD_I > 0.5$. They conclude that the spectrum

25 with positive BTD_I contains both volcanic ash and ice.

For the measured spectra in the left plot of Fig. 4, the corresponding ARTS/uvspec simulated spectra are shown in the right plot of Fig. 4. In the simulated spectra the O$_3$ and CO$_2$ absorption features centered at about 1050 cm^{-1} and below 768 cm^{-1}, respectively, have been left out to better visualize the broad band effects of ash and ice clouds. The ash mass loading, effective radius, ice water content and ice cloud top height used to simulate the various spectra, are listed in Table 1. These values were

30 those that gave the smallest RMSD compared with the measured spectra, see section 4.2.

The ice cloud spectrum is best modelled by an atmosphere including an ice cloud with top at 16 km and and ice water content of 0.2 g/m^3. The simulated cloudless spectrum also include an ice cloud at 16 km with a very low ice water content which has only a small effect on the brightness temperature, see also left plot of Fig. 5.

For the ash affected spectra the simulated spectra that gave the smallest RMSD for the ice only, ash only, and ash and ice cases, are shown in Fig. 6. Only the data points used to calculate the RMSD in Eq. 1 are shown. The ash only case (brown lines,
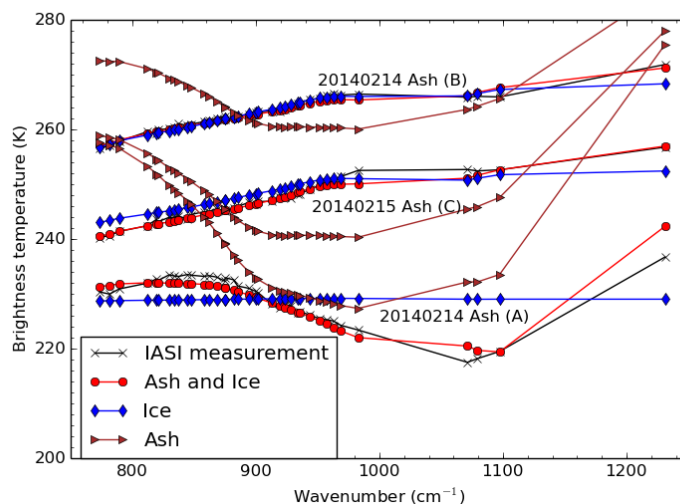
Figure 6. The brightness temperature for the pixels identified as ash in the right plots of Figs. 1 and 2, and marked as Ash (A,B,C) in left plot of Fig. 4 and in Table 1. The brightness temperature is shown only for points which are used to calculate the RMSD, Eq. 1. The various colors refers to the three cases described in section 4.2. Note that the lines connecting the points are drawn just for visualisation and do not represent the actual spectral behaviour between the data points.

Fig. 6) clearly does not reproduce the measured spectral behaviour (black lines, Fig. 6). The ice only case (blue lines, Fig. 6), does not reproduce the measured spectrum for Ash (A), but comes close for Ash (B) and Ash (C). However, for all the spectra
5   the ash and ice case (red lines, Fig. 6) best reproduce the measured spectra. Thus, the spectra said to include ash in the left plot of Fig. 4, are all best simulated by including both ash and ice clouds. For the spectra from 14 Feb the ash mass concentration is higher in the central parts of the plume, compare ash cases A and B in Table 1.

The large footprint of IASI is covered by several AVHRR/3 pixels. For the spectra in Fig. 4 the brightness temperatures in bands 4 (BT_4) and 5 (BT_5) of AVHRR/3 are shown versus each other in the right plot of Fig. 7. In the left plot of Fig. 7
10   is shown BT_4 versus $BT_4 - BT_5$. There is little variation in BT_4 for the cloudless and ice cloud cases as seen in Fig. 7 and in the sixth column of Table 1 which gives the standard deviation of BT_4 as 0.1 K for the cloudless and 1.1 K for the ice cloud cases. For the cases identified as ash the standard deviation is larger. Thus, the part of the atmosphere and underlying surface viewed by these IASI pixels are inhomogeneous and the IASI spectra represent the contributions from all these various atmospheric states. Thus, while discussing which modelled spectrum that best represents the measured spectrum, it must be
15   kept in mind that the measured spectrum represents an inhomogeneous atmosphere and the modelled derived values may thus not neccessarily represent the actual atmospheric state. Inhomogeneties in IASI footprints also affect other applications, for
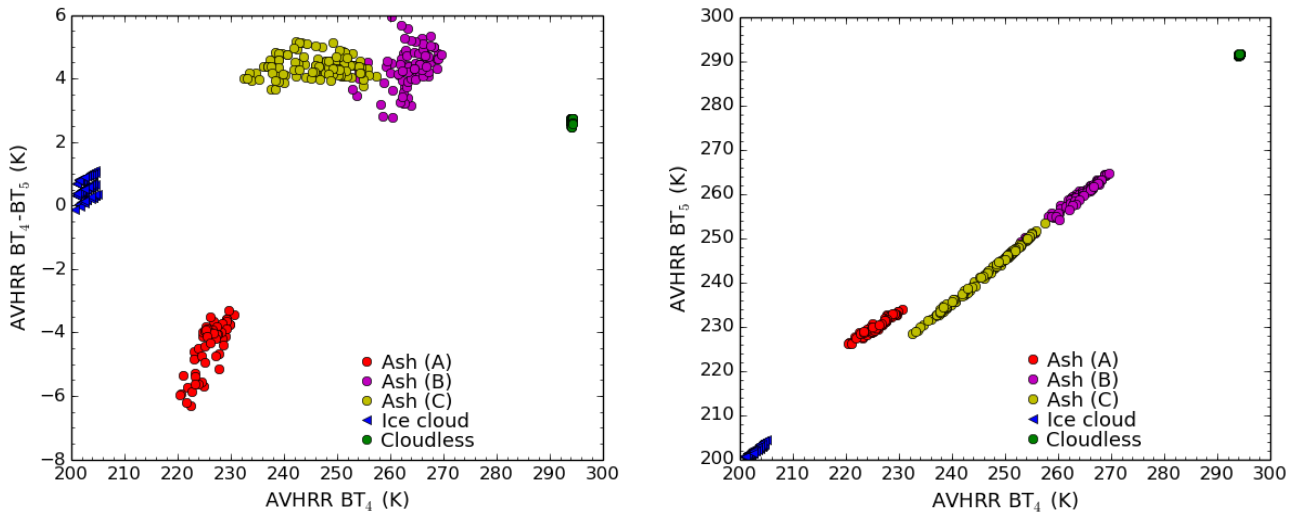
Figure 7. (Left plot) Measured AVHRR/3 BT_4 versus $BT_4 - BT_5$ for the pixels marked in the right plots of Figs. 1 and 2 and listed in Table 1. (Right plot) Measured AVHRR/3 BT_4 versus BT_5 for the same pixels as in left plot.

example current methods cannot correctly retrieve cloud pressures for multi-layer systems, which represents at least half of the cloudy situations recorded by IASI (Lavanant et al., 2011). Below the ash and ice clouds that best reproduced the IASI scenes in the right plots of Figs. 1 and 2 are presented.

5.3 Ash and ice clouds

5 The method presented in section 4.2 was used to estimate the ice and ash cloud properties that best reproduced the IASI spectra for the scenes shown in Figs 1 and 2. The ice water content, ice cloud height, and volcanic ash mass concentrations are shown together with the RMSD in Figs. 8 and 9 for 14 and 15 Feb, respectively. The frequencies of the ash mass loading and RMSD are shown in Fig. 10. The frequency of the RMSD is similar for pixels identified as ash and those not identified as ash, compare green and red bars in plots in columns 3 and 4, upper row, of Fig. 10, and also compare mean and standard deviation between

10 rows 1 and 2 and rows 5 and 6 in Table 2. Hence, when including modelled ash and ice, ash only and ice only spectra in the measurement-model comparison, the ash affected spectra are reproduced to a similar accuracy to those not affected by ash.

If the modelled spectra including both ash and ice are excluded from the comparison and the ash only and ice only included, the ash mass loading shifts to larger values as shown in the lower row of Fig. 10, plots in columns 1 and 2. Also the RMSD gets markedly worse, compare red bars in the bottom row, columns 3 and 4 plots of Figs. 10 with the red bars in the upper row,

15 and the mean and standard deviations of rows 2 and 4 and rows 6 and 8 in Table 2. Hence, modelled spectra including both ash and ice clouds better reproduce the measured ash affected spectra than using modelled spectra with ash only.
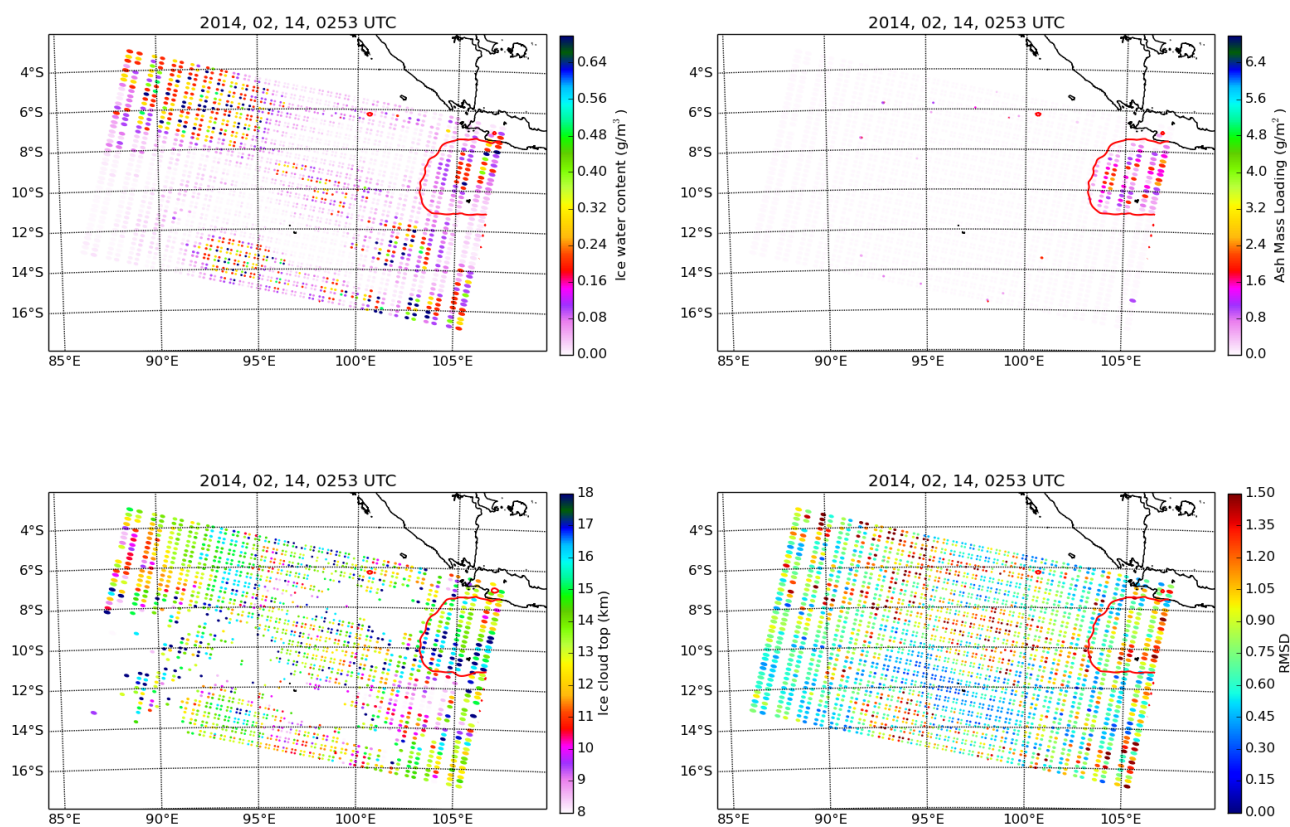
Figure 8. (Upper left plot) The estimated ice water content. (Upper right plot) The estimated ash mass loading. (Lower left plot) The estimated altitude of the ice cloud top height for ice clouds with ice water content >0.01 g/m². (Lower right plot) The root mean square difference (RMSD) of the simulated-measured spectra. The red contour line delineates the area identified as ash. Data from 14 Feb 2014, 0253 UTC.

If all ash identified pixels are to be reproduced with ice only spectra, the RMSD gets closer to the RMSD for the spectra including both ash and ice, compare red bars in the upper row, column 3 and 4 plots of Fig. 10 with blue bars in bottom row, and the mean and standard deviations of rows 2 and 3 and rows 6 and 7 in Table 2. While the mean and standard deviations in Table 2 are not too different, the improvement of using ash and ice spectra versus ice only spectra becomes clear when
5   comparing the RMSD for each pixel for the two approaches as shown in Fig. 11. If the two approaches had been of similar merit the data points would be symmetric around the 1:1 line. However, the RMSD is generally larger for the ice only case, hence generally the modelled spectra with both ash and ice better reproduce the measured spectra.

Table 2. The mean and standard deviation of the frequency distributions shown in Fig. 10.

Row	Description	Mean	Standard deviation
	14 Feb 2014		
1	All pixels (green bars, upper row, plot in column 3 of Fig. 10)	0.79	0.33
2	Ash only pixels (red bars, upper row, plot in column 3 of Fig. 10)	0.87	0.26
3	Ash only pixels assumed to be ice (blue bars, lower row, plot in column 3 of Fig. 10)	1.46	0.77
4	Ash only pixels assumed to be ash only (red bars, lower row, plot in column 3 of Fig. 10)	10.13	2.99
	15 Feb 2014		
5	All pixels (green bars, upper row, plot in column 4 of Fig. 10)	0.67	0.32
6	Ash only pixels (red bars, upper row, plot in column 4 of Fig. 10)	0.58	0.20
7	Ash only pixels assumed to be ice (blue bars, lower row, plot in column 4 of Fig. 10)	0.78	0.32
8	Ash only pixels assumed to be ash only (red bars, lower row, plot in column 4 of Fig. 10)	6.27	3.02

6 Discussion

Above it was shown that modelled spectra including both ash and ice clouds better reproduced the measured spectra. While considerably detail was included in the simulated spectra some of the limitations of the study are discussed here.

Water clouds and mixed phase clouds are not considered in this study. Hu et al. (2010) used combined CALIOP, Imaging Infrared Radiometer (IIR) and MODIS measurements to show that supercooled water clouds may be present for temperatures down to about -35° C. For the case studied here the temperature is below -35° C for altitudes larger than about 10 km. Here, all ice clouds are assumed to be 8 km or higher in altitude, but very few of the estimated ice cloud altitudes are below 10 km. It is noted that Hu et al. (2010) found very few supercooled clouds for latitudes between 40° S and 40° N which includes the area investigated here. On the other side the CALIOP data presented in Fig. 2e of Kristiansen et al. (2015) indicate some clouds around 5 km. However, to keep the computational burden managable, low altitude water clouds were not included in the analysis.

The ash was assumed to be andesite. A different composition will have a different refractive index which will change the spectral shape of the simulated spectra and hence may yield other ash and ice cloud estimates than those presented. Furthermore, the ash particles were assumed to be spherical. It has been shown by Kylling et al. (2014) that the assumption of spherical particle may underestimate the retrieved ash mass loading by tens of percent compared to porous non-spherical particles. Also, no internal mixing of ash and ice was included. However, external mixing of ash and ice was included when both clouds were at 18 km.

For all calculations the ash cloud was assumed to be at 18 km and 1 km thick. Moving the ash cloud up and down a few kilometers and changing its thickness will affect the results as demonstrated by Corradini et al. (2008). However, due to the computational burden, other ash clouds geometries were not considered.

The ice cloud particles were assumed to be solid columns with a mean effective radius of 40 μm. According to Faijan et al. (2012) ice particles shape and size change with location within the cloud with small, droxtals in the top, pristine hexagonal columns in the middle and larger irregular aggregates in the bottom layer. The uncertainty in crystal shape can lead to uncertainty in the brightness temperature of several Kelvins. Similar conclusions were made by Dubuisson et al. (2008) who investigated the effect of ice cloud microphysics on top of the atmosphere thermal radiation. Hyperspectral infrared sounders may be used to detect cloud microphysical properties. For example Li et al. (2005) retrieved cloud microphysical properties from MODIS and the Atmospheric Infrared Sounder (AIRS). However, no such attempt was made here. But it is noted that other ice cloud particle assumptions might yield different results.

SO_2 was also released during the eruption. While outside the scope of the present work, it would be of great interest to investigate how the presence of ash and/or ice clouds affects the SO_2 signature in the IASI spectra.

Scatter plot (not shown) of the ash mass loading versus the ice water content for the ash affected pixels show no correlation between the two. Thus, the ash and ice clouds appears to be independent of each other.

7 Conclusions

Two scenes during the Mt. Kelud February 2014 eruption have been studied using the hyperspectral IASI and broad band AVHRR/3 instruments onboard the Metop-A satellite. The instruments different capabilities to detect volcanic ash have been discussed and the spectral coverage of IASI explored to investigate the possible presence of both ice and volcanic ash. The main findings of the investigation are:

- The spectral coverage and resolution of the IASI instrument gives increased sensitivity to the presence of volcanic ash. As such, the use of IASI data for detection of volcanic ash is a powerful and attractive addition to the use of AVHRR/3 and similar instruments.

- IASI may detect ash when AVHRR/3 and similar instruments such as SEVIRI, MODIS and MTSAT, do not detect ash.

- Comparisons of modelled and measured IASI spectra suggests that during the Mt. Kelud 2014 eruption both ash and ice clouds were present simultaneously, but mostly at different altitudes.

- IASI may potentially retrieve both ash and ice clouds microphysical properties simultaneously.

- Underlying ice clouds reduce the ash needed to reproduce the measured IASI spectra by about a factor of 14 on the average.

Finally: in this study IASI spectra measured during the Mt. Kelud 2014 eruption were interpreted in terms of ash and ice clouds. It is noted that this interpretation does not rule out other interpretations based on other ash and ice and water cloud assumptions not considered here.

Acknowledgements. The Centre National d'Etudes Spatiales (CNES, France) developed and built IASI. It is flown onboard the Metop
5   satellites as part of the EUMETSAT Polar System. NILU receives IASI L1 data from Eumetsat through the EUMETCAST near real time
data distribution service. Part of this study was funded by the Norwegian Ministry of Transport and Communications.

References

Clarisse, L., Hurtmans, D., Prata, A. J., Karagulian, F., Clerbaux, C., Maziére, M. D., and Coheur, P.-F.: Retrieving radius, concentration, optical depth, and mass of different types of aerosols from high-resolution infrared nadir spectra, Appl. Opt., 49, 3713–3722, 2010a.

Clarisse, L., Prata, F., Lacour, J.-L., Hurtmans, D., Clerbaux, C., and Coheur, P.-F.: A correlation method for volcanic ash detection using hyperspectral infrared measurements, Geophys. Res. Lett., 37, doi:10.1029/2010GL044 828, 2010b.

Clarisse, L., R'Honi, Y., Coheur, P.-F., Hurtmans, D., and Clerbaux, C.: Thermal infrared nadir observations of 24 atmospheric gases, Geophysical Research Letters, 38, n/a–n/a, doi:10.1029/2011GL047271, http://dx.doi.org/10.1029/2011GL047271, 2011.

Clarisse, L., Coheur, P.-F., Prata, F., Hadji-Lazaro, J., Hurtmans, D., and Clerbaux, C.: A unified approach to infrared aerosol remote sensing and type specification, Atmospheric Chemistry and Physics, 13, 2195–2221, doi:10.5194/acp-13-2195-2013, http://www.atmos-chem-phys.net/13/2195/2013/, 2013.

Clerbaux, C., Boynard, A., Clarisse, L., George, M., Hadji-Lazaro, J., Herbin, H., Hurtmans, D., Pommier, M., Razavi, A., Turquety, S., Wespes, C., and Coheur, P.-F.: Monitoring of atmospheric composition using the thermal infrared IASI/MetOp sounder, Atmospheric Chemistry and Physics, 9, 6041–6054, doi:10.5194/acp-9-6041-2009, http://www.atmos-chem-phys.net/9/6041/2009/, 2009.

Corradini, S., Spinette, C., Carboni, E., Tirelli, C., Buongiorno, M. F., Pugnaghi, S., and Gangale, G.: Mt. Etna tropospheric ash retrieval and sensitivity analysis using Moderate Resolution Imaging Spectroradiometer Measurements, J. of Applied Remote Sensing, 2, doi:10.1117/1.3046 674, 2008.

DeSouza-Machado, S. G., Strow, L. L., Hannon, S. E., and Motteler, H. E.: Infrared dust spectral signatures from AIRS, Geophys. Res. Lett., 33, doi:doi:10.1029/2005GL024364, 2006.

Dubuisson, P., Giraud, V., Pelon, J., Cadet, B., and Yang, P.: Sensitivity of thermal infrared radiation at the top of the atmosphere and the surface to ice cloud microphysics, J. of Applied Meteorology and Climatology, 47, 2545–2560, 2008.

Emde, C., Buras-Schnell, R., Kylling, A., Mayer, B., Gasteiger, J., Hamann, U., Kylling, J., Richter, B., Pause, C., Dowling, T., and Bugliaro, L.: The libRadtran software package for radiative transfer calculations (Version 2.0), Geoscientific Model Development Discussions, 8, 10 237–10 303, doi:10.5194/gmdd-8-10237-2015, http://www.geosci-model-dev-discuss.net/8/10237/2015/, 2015.

Eriksson, P., Buehler, S. A., Davis, C. P., Emde, C., and Lemke, O.: ARTS, the atmospheric radiative transfer simulator, version 2, J. Quant. Spectrosc. Radiat. Transfer, 112, 1551–1558, 2011.

Faijan, F., Lavanant, L., and Rabier, F.: Towards the use of cloud microphysical properties to simulate IASI spectra in an operational context, Journal of Geophysical Research: Atmospheres, 117, n/a–n/a, doi:10.1029/2012JD017962, http://dx.doi.org/10.1029/2012JD017962, d22205, 2012.

Gangale, G., Prata, A. J., and Clarisse, L.: The infrared spectral signature of volcanic ash determined from high-spectral resolution satellite measurements, Remote Sens. Environ., 114, 414–425, 2010.

Hilton, F., Armante, R., August, T., Barnet, C., Bouchard, A., Camy-Peyret, C., Capelle, V., Clarisse, L., Clerbaux, C., Coheur, P.-F., Collard, A., Crevoisier, C., Dufour, G., Edwards, D., Faijan, F., Fourrié, N., Gambacorta, A., Goldberg, M., Guidard, V., Hurtmans, D., Illingworth, S., Jacquinet-Husson, N., Kerzenmacher, T., Klaes, D., Lavanant, L., Masiello, G., Matricardi, M., McNally, A., Newman, S., Pavelin, E., Payan, S., Péquignot, E., Peyridieu, S., Phulpin, T., Remedios, J., Schlüssel, P., Serio, C., Strow, L., Stubenrauch, C., Taylor, J., Tobin, D., Wolf, W., and Zhou, D.: Hyperspectral Earth Observation from IASI: Five Years of Accomplishments, Bulletin of the American Meteorological Society, 93, 347–370, doi:10.1175/BAMS-D-11-00027.1, http://dx.doi.org/10.1175/BAMS-D-11-00027.1, 2011.

Hu, Y., Rodier, S., Xu, K.-m., Sun, W., Huang, J., Lin, B., Zhai, P., and Josset, D.: Occurrence, liquid water content, and fraction of super-cooled water clouds from combined CALIOP/IIR/MODIS measurements, Journal of Geophysical Research: Atmospheres, 115, n/a–n/a, doi:10.1029/2009JD012384, http://dx.doi.org/10.1029/2009JD012384, 2010.

Key, J. R., Yang, P., Baum, B. A., and Nasiri, S. L.: Parameterization of shortwave ice cloud optical properties for various particle habits, J. Geophys. Res., 107, doi:10.1029/2001JD000 742, 2002.

Kristiansen, N. I., Prata, A. J., Stohl, A., and Carn, S. A.: Stratospheric volcanic ash emissions from the 13 February 2014 Kelut eruption, Geophysical Research Letters, 42, 588–596, doi:10.1002/2014GL062307, http://dx.doi.org/10.1002/2014GL062307, 2014GL062307, 2015.

Kylling, A., Kahnert, M., Lindqvist, H., and Nousiainen, T.: Volcanic ash infrared signature: porous non-spherical ash particle shapes compared to homogeneous spherical ash particles, Atmospheric Measurement Techniques, 7, 919–929, doi:10.5194/amt-7-919-2014, http://www.atmos-meas-tech.net/7/919/2014/, 2014.

Lavanant, L., Fourrié, N., Gambacorta, A., Grieco, G., Heilliette, S., Hilton, F. I., Kim, M.-J., McNally, A. P., Nishihata, H., Pavelin, E. G., and Rabier, F.: Comparison of cloud products within IASI footprints for the assimilation of cloudy radiances, Quarterly Journal of the Royal Meteorological Society, 137, 1988–2003, doi:10.1002/qj.917, http://dx.doi.org/10.1002/qj.917, 2011.

Li, J., Huang, H.-L., Liu, C.-Y., Yang, P., Schmit, T. J., Wei, H., Weisz, E., Guan, L., and Menzel, W. P.: Retrieval of cloud microphysical properties from MODIS and AIRS, J. of Applied Meteorology, 44, 1526–1543, 2005.

Maddy, E. S., King, T. S., Sun, H., Wolf, W. W., Barnet, C. D., Heidinger, A., Cheng, Z., Goldberg, M. D., Gambacorta, A., Zhang, C., and Zhang, K.: Using MetOp-A AVHRR Clear-Sky Measurements to Cloud-Clear MetOp-A IASI Column Radiances, Journal of Atmospheric and Oceanic Technology, 28, 1104–1116, doi:10.1175/JTECH-D-10-05045.1, http://dx.doi.org/10.1175/JTECH-D-10-05045.1, 2011.

Mayer, B. and Kylling, A.: Technical note: the libRadtran software package for radiative transfer calculations-description and examples of use, Atmos. Chem. Phys., 5, 1855–1877, 2005.

Pollack, J. B., Toon, O. B., and Khare, B. N.: Optical properties of some terrestrial rocks and glasses, ICARUS, 19, 372–389, 1973.

Prata, A. J.: Infrared radiative transfer calculations for volcanic ash clouds, Geophys. Res. Lett., 16, 1293–1296, 1989.

Schlüssel, P., Hultberg, T. H., Phillips, P. L., August, T., and Calbet, X.: The operational {IASI} Level 2 processor, Advances in Space Research, 36, 982 – 988, doi:http://dx.doi.org/10.1016/j.asr.2005.03.008, http://www.sciencedirect.com/science/article/pii/S0273117705002838, atmospheric Remote Sensing: Earth's Surface, Troposphere, Stratosphere and Mesosphere- I, 2005.

Snyder, W. C., Wan, Z., Zhang, Y., and Feng, Y.-Z.: Thermal Infrared (3-14 μm) bidirectional reflectance measurements of sands and soils, Remote Sensing of Environment, 60, 101 – 109, doi:http://dx.doi.org/10.1016/S0034-4257(96)00166-6, http://www.sciencedirect.com/science/article/pii/S0034425796001666, 1997.

Wen, S. and Rose, W. I.: Retrieval of sizes and total masses of particles in volcanic clouds using AVHRR bands 4 and 5, J. Geophys. Res., 99, 5421–5431, 1994.

Yang, P., Liou, K. N., Wyser, K., and Mitchell, D.: Parameterization of the scattering and absorption properties of individual ice crystals, J. Geophys. Res., 105, 4699–4718, 2000.
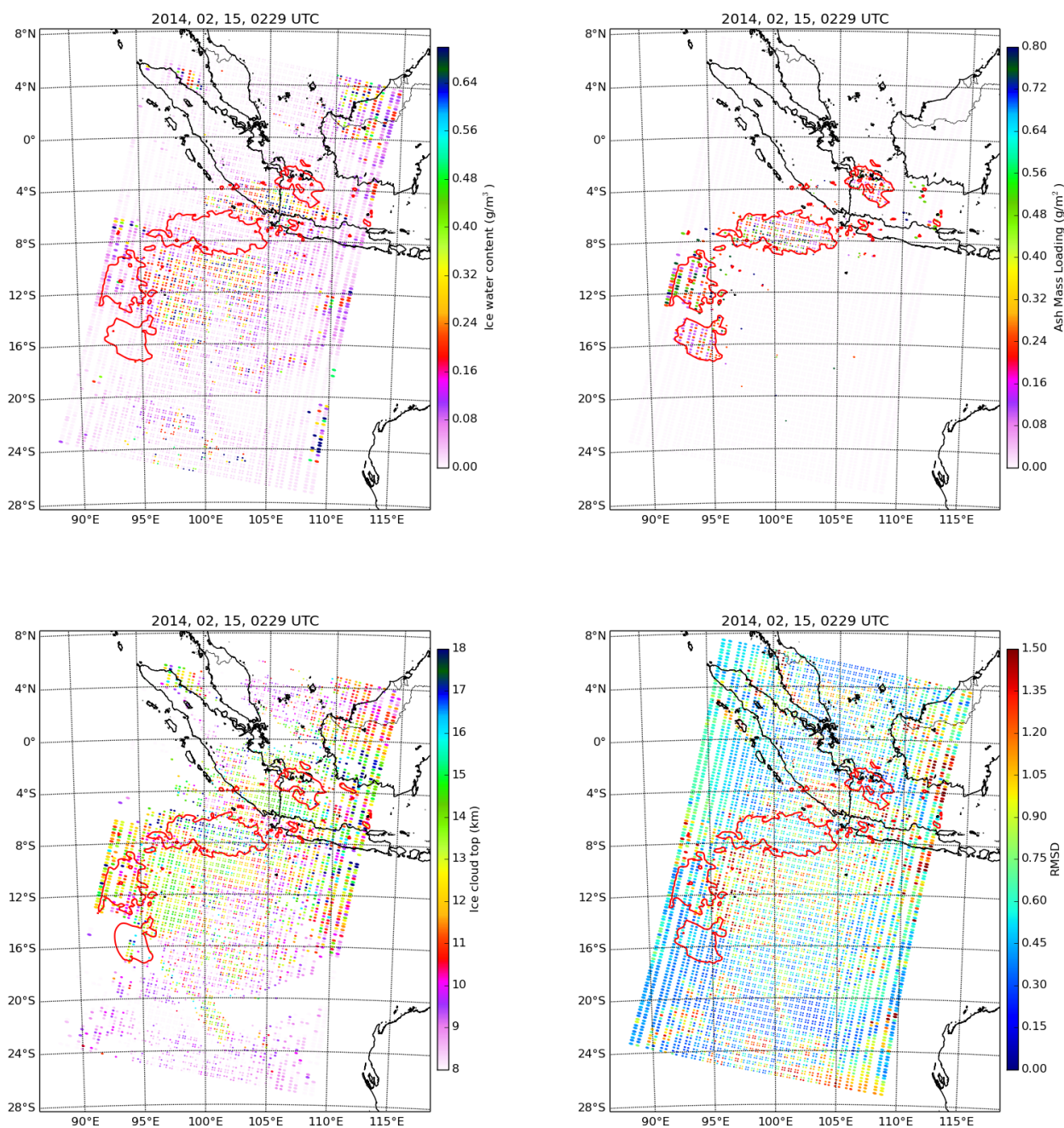
Figure 9. (Upper left plot) The estimated ice water content. (upper right plot) The estimated ash mass loading. (lower left plot) The estimated altitude of the ice cloud top. height for ice clouds with ice water content >0.01 g/m^2. (lower right plot) The root mean square difference (RMSD) of the simulated-measured spectra. The red contour line delineates the area identified as ash. Data from 15 Feb 2014, 0229-0235 UTC.
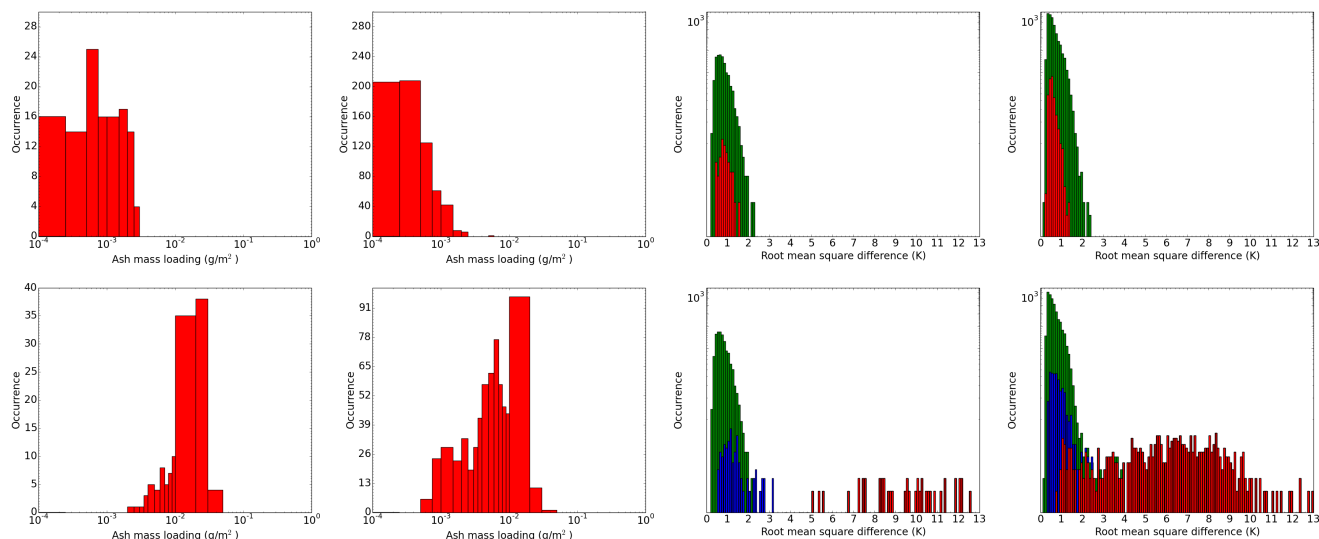
Figure 10. (Upper row) The frequency of the ash mass loading (columns 1 and 2) and the RMSD (columns 3 and 4) when including all types of simulated spectra. (Lower row) The frequency of the ash mass loading (columns 1 and 2) and the RMSD (columns 3 and 4) when not including spectra with both ash and ice. In columns 3 and 4 the red bars represents ash affected pixels while the green bars are all other pixels. In the lower row the blue bars represents the ash affected pixels but modelled ice spectra were used to calculate the RMSD, see text for details. Note log-scale on y-axis for plots in columns 3 and 4. Columns 1 and 3: data from 14 Feb 2014. Columns 2 and 4: data from 15 Feb 2014.
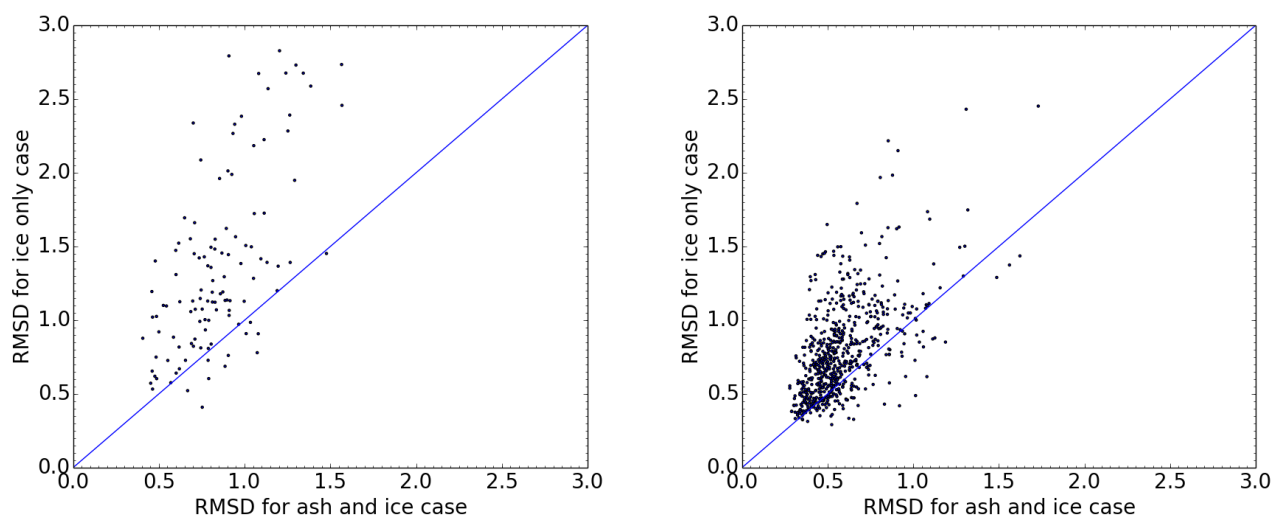
Figure 11. The RMSD for the ash and ice case versus the ice only case for 14 Feb 2014 (lef plot) and 15 Feb 2014 (right plot).